Photoisomerization of phytochrome chromophore models: An XMS-CASPT2 study

Author affiliation:

Aditya G. Rao[a] and Igor Schapiro[a]

[a]Fritz Haber Center for Molecular Dynamics Research, Institute of Chemistry, The Hebrew University of Jerusalem, Jerusalem 91904, Israel

Corresponding author:

Dr. Igor Schapiro

Fritz Haber Center for Molecular Dynamics Research,

Institute of Chemistry,

The Hebrew University of Jerusalem,

Jerusalem 91904, Israel

Email: igor.schapiro@mail.huji.ac.il

Keywords: linear tetrapyrrole**,** photoisomerization, conical intersection, XMS-CASPT2, phytochrome

Abstract

Phytochromes are a superfamily of photoreceptors that harbor linear tetrapyrroles as chromophores. Upon light illumination, the linear tetrapyrrole chromophore undergoes a double bond isomerization which starts a photocycle. In this work, we studied the photoisomerization of chromophore models designed based on the C- and D-rings of the phycocyanobilin (PCB) chromophore. In total, five different models with varying substitutions were investigated. Firstly, the vertical excitation energies were benchmarked using different computational methods to establish the relative order of the excited states. Based on these calculations, we computed the photoisomerization profiles using the extended multi-state (XMS) version of the CASPT2 method. The profiles were obtained for both the clockwise and counterclockwise rotations of the $C_{15} = C_{16}$ bond in the *Z* and *E* isomers using a linear interpolation of internal coordinates between the Franck-Condon and MECI geometries. In the minimal chromophore model that lacks the substitutions at the pyrrole rings, the isomerization involves both $C_{14} - C_{15}$ and $C_{15} = C_{16}$ bonds of the methine bridge between the C- and D-rings, resembling the hula-twist motion. The MECIs are characterized by a partial charge transfer between the two pyrrole rings pointing towards a twisted intramolecular charge transfer. Systematic introduction of substituents leads to an increase in the steric repulsion between the two pyrrole rings causing a pretwist of the dihedral around the $C_{15} = C_{16}$ bond, which creates a preference for the counterclockwise isomerization. Upon introduction of the carbonyl group at the D-ring the charge transfer has increased. This changes the isomerization mechanism from hula-twist to one-bond flip.

Introduction

Phytochromes constitute a superfamily of photoreceptor proteins that are present in plants, bacteria and fungi.[1] The photoreceptor core has a unique three domain architecture consisting of PAS, GAF and PHY domains (Fig. 1). A linear tetrapyrrole chromophore is bound to a conserved cysteine residue within the GAF domain (Fig. 1). Depending on the organism, the chromophore can vary between biliverdin (BV), phycocyanobilin (PCB), phytochromobilin (PΦB) and phycoviolobilin (PVB) (Fig. 2).[2] The differences between these tetrapyrroles are highlighted in orange in Fig 2. Despite the numerous classes of phytochromes from different organisms and the variations in their chromophores, the primary event is the light-induced isomerization that proceeds around the $C_{15} = C_{16}$ bond located in the methine bridge between the C- and D- pyrrole rings of the chromophore.

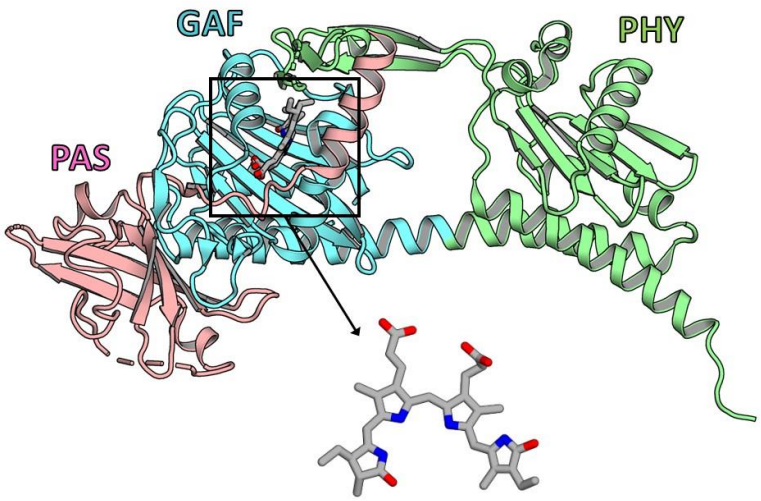

Fig 1. Cyanobacterial Phytochrome (Cph1) with PCB as the chromophore. The three domains PAS, GAF and PHY are colored accordingly.

Typically a double bond photoisomerization is initiated by an excitation from the ground state minimum to the Franck-Condon (FC) point of an excited state. Further, relaxation on the excited state occurs by twisting the double bond. As the twisting approaches 90° the excited and the ground states become degenerate, ultimately leading to a conical intersection (CI).[3,4] A CI serves as a non-radiative decay channel for the excited state population to the ground state (Fig. 3). This results in the formation of the primary photoproduct which usually is complete on the

femtosecond to picosecond timescale depending on the presence of a barrier. However, it is unclear how this general description of the photoisomerization is transferred to linear tetrapyrrole chromophores. To address this issue, we have applied computational methods to explore the excited state topology, locate the CI and characterize the initial excited state relaxation of linear tetrapyrrole models.

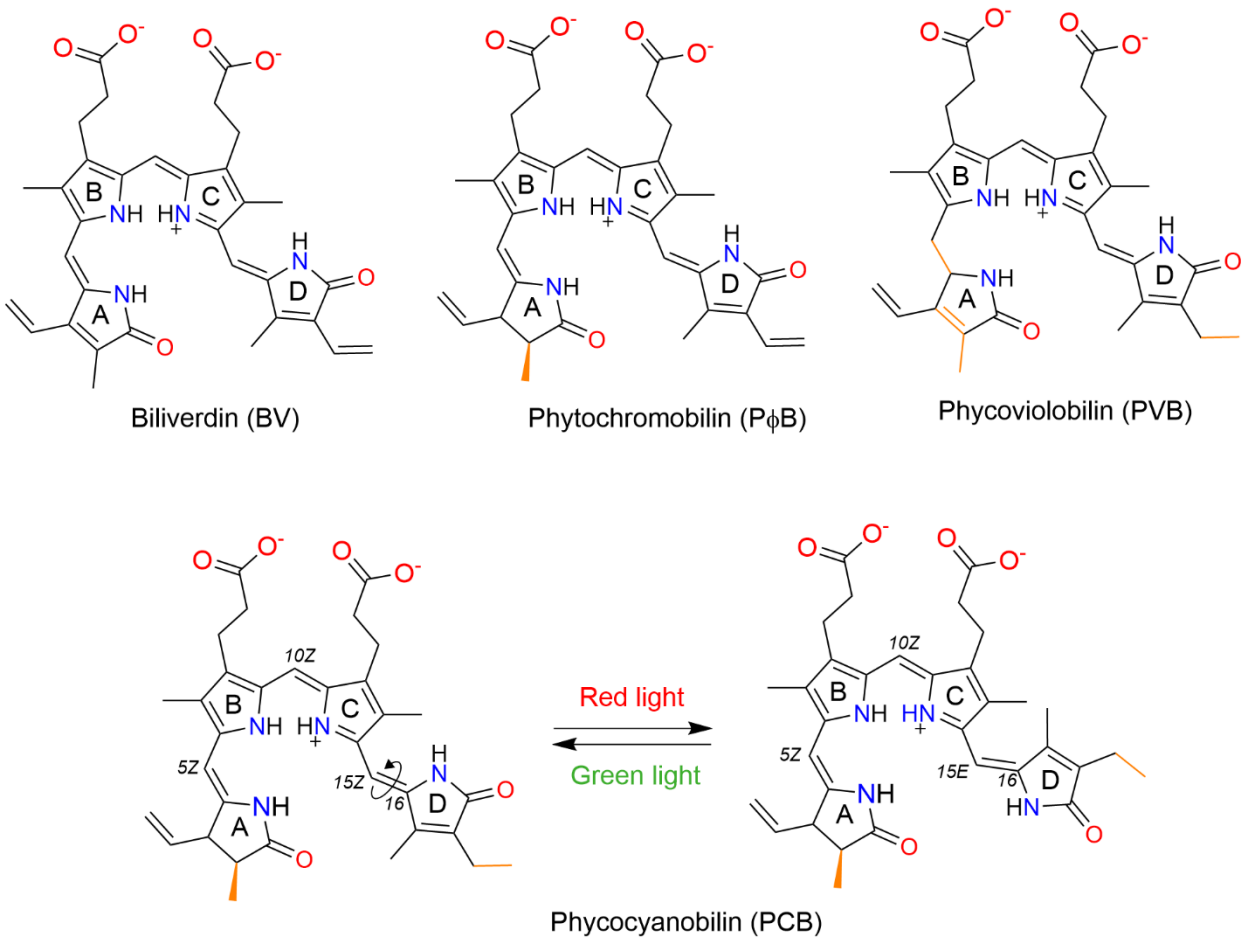

Fig. 2 Molecular structures of tetrapyrroles found in phytochromes. The isomerization scheme is shown only for PCB.

A plethora of experimental spectroscopic studies[5–10] have been used to characterize the primary step in the phytochrome photochemistry. Computational studies, however, are scant compared to other photoreceptor proteins. This is due to the large size of the chromophore and the associated computational demand when using highly correlated methods to describe the full π-system. By employing computationally feasible linear response TD-DFT (LR-TD-DFT), Durbeej and co-workers[11,12] computed excited state relaxed scans for the full BV chromophore along

different torsion angles. Although LR-TD-DFT is a cost-effective approach in describing vertical excitation energies, it is a single-reference method and fails to describe the portion of the potential energy surface near the CI.[13,14]

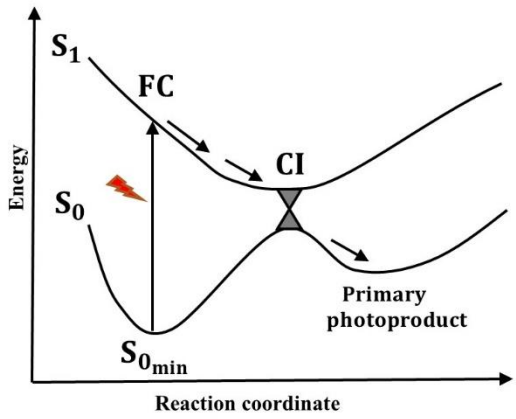

Fig. 3 Model potential energy surface of the photoisomerization in phytochromes.

Multiconfigurational wave function based methods were designed to describe the topology of such crossings between different electronic states.[15] The widely used multiconfigurational wave function method Complete Active Space Self Consistent Field (CASSCF) has been applied to other chromophores from photoreceptor proteins.[4,16,17] The CASSCF method requires a selection of an active space which typically comprises the full π-system of a chromophore. However, for the BV chromophore an active space of 32 electrons in 29 orbitals is required.[18] Such an active space size is computationally intractable since the maximum size currently achievable is 18 electrons in 18 orbitals.[19] Therefore, in previous studies a compromise was chosen to either employ approximate electronic structure methods, such as a semi-empirical method,[20–22] or to truncate the chromophore.[23–28] In the latter approach, typically, the propionic acid groups[23] are replaced by hydrogen atoms because they are not part of the conjugated π-system. Other strategies to reduce the model size include removal of methyl groups[24,25] or even truncation of the pyrrole rings.[26,27] Zietz and Blomgren[28] used the CASSCF method with varying active spaces to locate CIs on a truncated model comprising of two pyrrole rings in the gas phase. They found that the calculated CIs were 12 kcal·mol^{-1} lower in energy than the FC point and can be reached by a concerted twist of the $C_{14} - C_{15}$ and $C_{15} = C_{16}$ bonds. Klan and coworkers[29] used CASSCF with a minimal active space of 2 electrons in 2 orbitals to study the nonadiabatic dynamics of a dipyrrinone unit. A larger

model of the PΦB chromophore was used by Garavelli and co-workers[30] in the gas phase to compute relaxed scans in the excited state using CASPT2//CASSCF(10,11) methodology. They found that the $C_9 - C_{10}$ and $C_{10} = C_{11}$ bonds of the central methine bridge have a higher preference for isomerization. A similar finding was obtained by Lan and coworkers[20], who used the semiempirical method OM2/MRCI for carrying out non-adiabatic dynamics. As exemplified by the latter two studies, it is clear that several photochemical channels exist in the gas phase through which the chromophore decays to the ground state. However, the isomerization of the $C_{15} = C_{16}$ bond between the C- and D-rings is exclusively observed in experiments or crystal structures of the photoproducts[31], signifying the cruciality of the protein environment in the photoisomerization.

Recently, computational studies of the photoisomerization taking into effect explicit interaction of the protein environment using hybrid QM/MM techniques were reported. Using RI-ADC(2), Slavov et al[32] reported excited state relaxed scans for a phytochrome-like GAF domain namely all2699g1 that harbors PCB as the chromophore. In this study, it was shown that the protein environment induces a preference for counterclockwise rotation of the D-ring compared to a clockwise motion. This is consistent with the recent QM/MM non-adiabatic molecular dynamics (NAMD) study by Groenhof and coworkers[33] with SA2-CASSCF/3-21G as the QM level of theory on the *Deinococcus radiodurans* phytochrome. For the same phytochrome, Mennucci and coworkers[22] carried out non-adiabatic molecular dynamics. They observed a concerted rotation of a single and double bond, which is known as a hula-twist isomerization mechanism. This isomerization was found to have a preference for the counterclockwise rotation of the D-ring.

The main focus of this work is to apply a highly accurate quantum chemical method to study the excited state potential energy surface including the CI. To this end, we used the Complete Active Space Perturbation Theory (CASPT2) method, which is a multireference second-order perturbation theory applied on top of the CASSCF method. The benefit of CASPT2 is that it can recover the dynamic electron correlation which is missing in CASSCF. Recently, the analytic gradients became available for CASPT2[34,35] making geometry optimizations feasible. Due to the high computational cost, we used a tetrapyrrole model of two pyrrole rings. This permits to include the full π-system in the active space. It also allowed us to avoid the loss in selectivity of the isomerizing bond which was observed in previous gas phase studies[23]. Further, we analyzed the contribution of the functional groups by systematically introducing substitutions to the C-D

dipyrrole model. We computed excited state profiles for both 15-*Z* and 15-*E* isomers because they may exhibit different photochemical paths (Fig. 2). An additional motivation for the use of truncated models is that we can apply the accurate XMS-CASPT2 method, which is too demanding for the entire chromophore. Therefore our results can be used as a benchmark for affordable electronic structure methods such as LR-TD-DFT or algebraic diagrammatic construction to second order (ADC(2)).

Recently, truncated tetrapyrrole models have been also studied experimentally.[27,29,36–38] Ultrafast spectroscopy experiments of model chromophores in solution have been reported. These experiments have found an ultrafast relaxation of the chromophore where the isomerization takes place on a picosecond timescale. However, the models in the latter studies are not identical to the models described in this study and the differences are discussed in the following section.

This paper is organized as follows: Firstly, we compared the vertical excitation energies of all the dipyrrole models in both the 15-*Z* and 15-*E* isomers. Then we determined the minimum energy conical intersection (MECI) geometries. Finally, we discussed the photoisomerization profiles obtained by a linear interpolation of internal coordinates (LIIC) between the FC and the respective MECI geometries.

Computational Methodology

Model compounds. Several models of the linear tetrapyrrole chromohores were reported in the literature. Zietz and Blomgren[28] used a dipyrrinone (DPN) model of bilirubin where all the alkyl groups were replaced by hydrogen atoms. Dean and coworkers[27] reported a combined spectroscopic and computational study of two truncated models: DPN and dipyrrole (DPY). However, the DPN model is structurally different from the one studied by Zietz and Blomgren[28], as the former was designed to mimick the A-/B- or C-/D- rings of bilirubin. The DPY model was designed to mimic the B- and C-rings of phycourobilin (PUB). Three different conformations of the DPN and DPY models were studied. Klan and coworkers[29,37] measured transient absorption spectra of a fragment of bilirubin containing the C- and D-rings with the functional groups as found in bilirubin. In all these studies discussed above, only the DPY model of Dean and coworkers[27] is positively charged, while all the other chromophores are neutral.

In this work we are interested in studying the photoisomerization of the D-ring in linear tetrapyrrole chromophores, therefore our models comprise only the pyrrole rings C and D. In the minimal model the carbonyl and methyl groups are substituted by hydrogens. This model is named "DPY − CD_{min}" (Fig. 4) to avoid confusion with the aforementioned models. The propionate chain at the C-ring was replaced by a hydrogen atom. Hence, this model has a net positive charge. Three additional models were obtained by systematically increasing the size and complexity of the substituents. The introduction of methyl and methylidene groups resulted in the "DPY − CD" and "DPY − CD_{CH_2}" models, respectively. The addition of a carbonyl group to the minimal model and the DPY − CD model, resulted in the "DPN − CD_{min}" and "DPN − CD" model, respectively. The DPN − CD model resembles the C-D dipyrrole subunit of the PCB chromophore. We have calculated both the *Z* and *E* isomers of the $C_{15} = C_{16}$ bond for all the models. An overview of all the models in our study is given in Fig. 4. The numbering of the atoms in the models is identical to the full chromophore (Fig. 2).

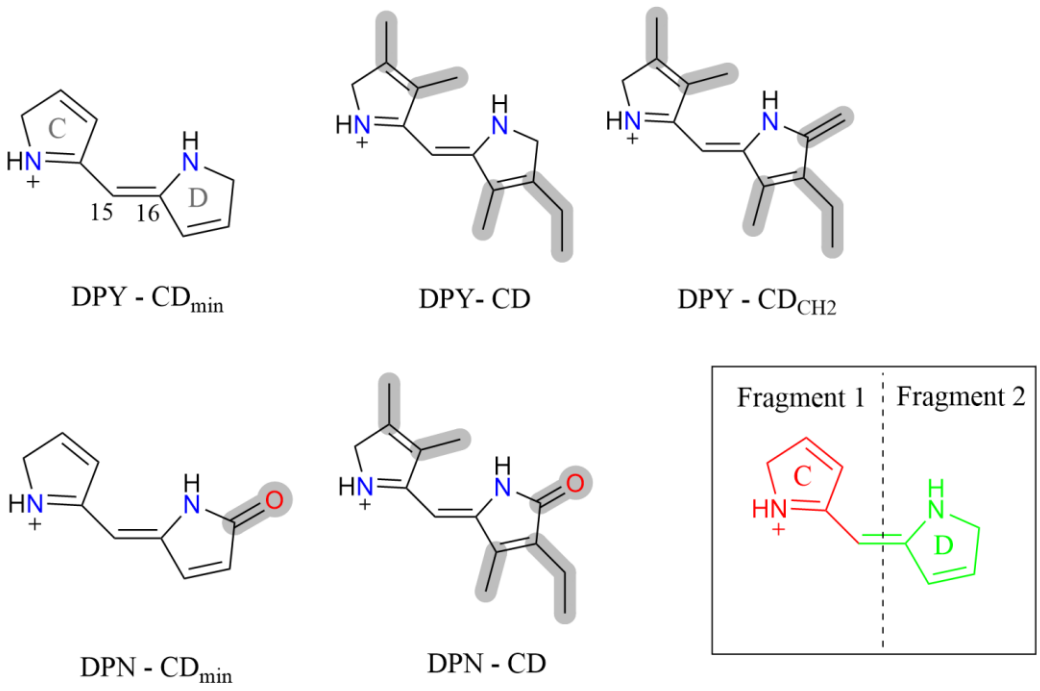

Fig. 4. Overview of the chromophore models studied in this work. The figure in the inset represents the fragmentation scheme used to calculate the Mulliken charge distribution

Active space selection. The choice of the active space depends on the model size. The models lacking the carbonyl and the methylidene groups namely $\mathrm{DPY-CD_{min}}$ and $\mathrm{DPY-CD}$ were described by an active space of 10 electrons in 9 orbitals (10,9) accounting for all the π-type orbitals. For the model including the methylidene group, namely $\mathrm{DPY-CD_{CH_2}}$, an additional double bond increases the active space to 12 electrons in 11 orbitals (12,11). For $\mathrm{DPN-CD_{min}}$ and $\mathrm{DPN-CD}$ models, which have a carbonyl group, the latter active space was augmented by 2 electrons and the corresponding lone pair orbital at the oxygen atom, resulting in a CAS of 14 electrons in 12 orbitals (14,12). The active space orbitals for the largest model ($\mathrm{DPN-CD}$) is shown in Fig. 5.

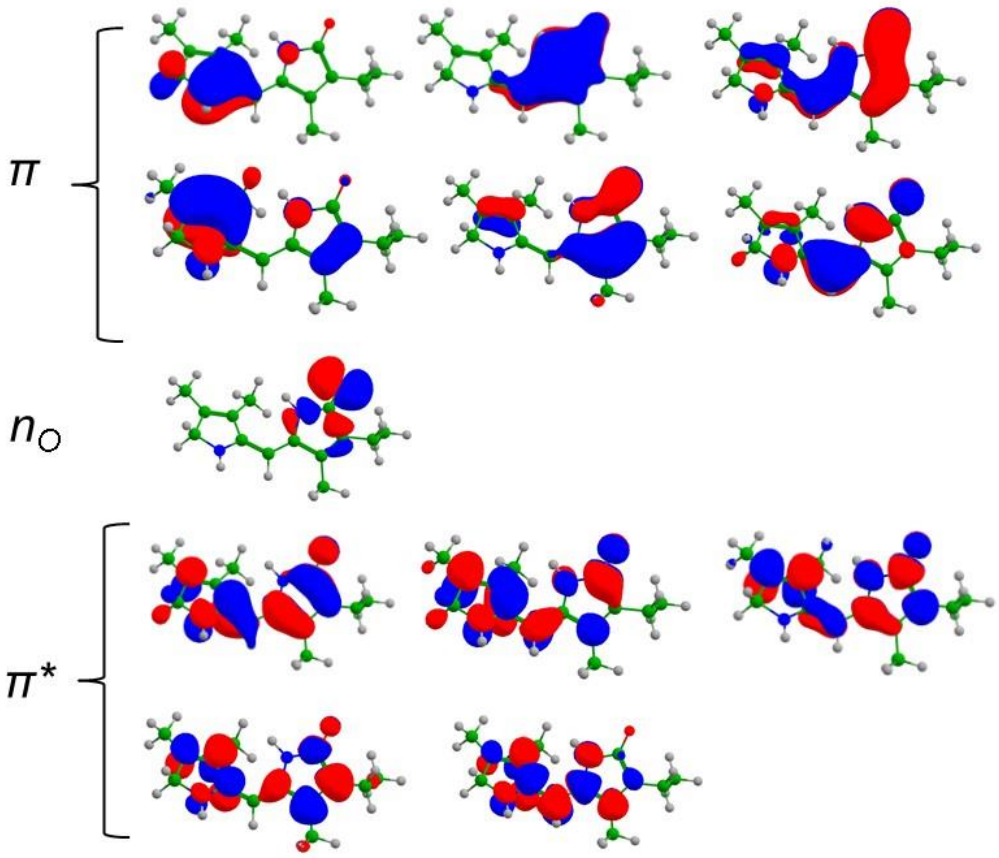

Fig. 5. Active space orbitals (14,12) for the $\mathrm{DPN-CD}$ model used in the XMS-CASPT2 calculations.

Ground state optimization and vertical excitation energies. In the calculations of the vertical excitation energies three states were averaged in the CASSCF wave function. The dynamic electron correlation was recovered by a subsequent CASPT2 calculation in the extended multistate

(XMS) formalism. A level shift parameter of 0.2 E_h was employed to overcome the problem of intruder states in the XMS-CASPT2 calculations. The basis set used in all calculations was def2-SVP which was chosen to be a trade-off between computational cost and accuracy. The truncated models were optimized on the ground state using XMS-CASPT2 in ChemShell[39] interfaced to the BAGEL[34] program.

Vertical excitation energies were also assessed by computing five excited states using TD-DFT and ADC(2) methods which do not require a selection of the active space. A range separated hybrid functional, CAM-B3LYP[40] with and without employing the Tamm-Dancomff approximation (TDA) was used. These calculations were done with dispersion correction and Becke-Johnson damping (D3BJ). ADC(2) was used in the resolution of identity formulation (RI-ADC(2)).[41] In addition, we have used two variants of ADC(2) namely Spin-Component-Scaled (SCS-ADC(2) and Spin-Opposite-Scaled (SOS-ADC(2))[42]. Both methods use scaling parameters for the same-spin and opposite-spin contributions. The recommended parameters of 1.200 and 0.333 were used for the opposite and same-spin components, respectively, in the SCS-ADC(2)[43]calculation. Whereas for SOS-ADC(2)[44] the corresponding parameters were 1.300 and 0.000, respectively. The TD-DFT and ADC(2) calculations were done in Gaussian09[45] and Turbomole 7.3[46], respectively.

Photoisomerization profile. The MECIs were computed in both clockwise and counterclockwise pathways by optimizing the CI between the S_1 excited and ground state using XMS-CASPT2. Typically, this requires the computation of both non-adiabatic coupling vectors (NAC) and analytic gradients of the electronic states.[47] However, we performed the CI optimization using the CIOpt[48] program since it does not require the NACs and works for any method that is able to compute energies for the electronic states of interest. A LIIC between the FC point and MECI geometries was computed using the Columbus program.[49–51]

In addition, excited state relaxed scans at the XMS-CASPT2 level were done for all the models starting from a CASSCF optimized ground state geometry. The scans were computed by rotating the $C_{14} - C_{15} = C_{16} - N_D$ dihedral (hereafter called ϕ_D where *D* stands for double bond) in steps of 10° in both counterclockwise and clockwise directions. At each step, a constrained optimization was done on the excited state by fixing ϕ_D and relaxing all other degrees of freedom. These calculations employed a CAS(10,9) for $\mathrm{DPY-CD_{min}}$ and $\mathrm{DPY-CD}$ models, while an active space CAS(12,11) for the $\mathrm{DPY-CD_{CH_2}}$, $\mathrm{DPN-CD_{min}}$ and $\mathrm{DPN-CD}$ models. Due to the high

computational demand of excited state geometry optimization at the XMS-CASPT2 level, we have omitted the lone pair orbital on the carbonyl oxygen atom of the DPN models. Consequently, the nπ* state was also omitted and only two states were averaged in the CASSCF wave function. This is justified by the immediate separation between the ππ* and the nπ* state as described in the LIICs below.

Mulliken charge distribution. To analyze the changes in the charge distribution, Mulliken charges were computed from the relaxed density matrices at the XMS-CASPT2 level of theory. The dipyrrole models were divided into two fragments where fragment 1 consists of the C-ring and the linking methine bridge while fragment 2 consists of the D-ring (Fig 4). The sum of atomic charges was calculated for each fragment.

Results

Vertical excitation energies. The XMS-CASPT2 excitation energies are presented in Fig. 6. In the models lacking the carbonyl group, the S_1 state is dominated by a ππ*-type transition. Introduction of a carbonyl group ($\mathrm{DPN-CD_{min}}$ and $\mathrm{DPN-CD}$) leads to an additional state with nπ* character in close proximity (<0.24 eV) to the spectroscopically bright ππ* transition. For the $\mathrm{DPN-CD_{min}}$ model the nπ* state is lower in energy than the ππ* state.

In addition to XMS-CASPT2, we computed the excitation energies using the black box methods ADC(2) and TD-CAM-B3LYP. The ADC(2) excitation energies (Fig. S1 and Table S1) corresponding to the ππ* transition are slightly higher (~0.1-0.2 eV) than the XMS-CASPT2 counterparts (Fig. 6), with the exception of the $\mathrm{DPY-CD_{CH_2}}$ model. However, at the ADC(2) level of theory, the nπ* state is lower than ππ* state for the DPN-type models with the exception of the $E-\mathrm{DPN-CD}$ model. In contrast to XMS-CASPT2, the energy gap between the nπ* and the ππ* states is larger for $\mathrm{DPN-CD_{min}}$ than for $\mathrm{DPN-CD}$ models at the ADC(2) level of theory. The SOS and SCS variants of ADC(2) remediate the order of these two states (Fig. S2 and S3).For the $\mathrm{DPN-CD_{min}}$ model the $\mathrm{S_1}$and $\mathrm{S_2}$ are nearly degenerate as the energy difference is below 0.05 eV at the XMS-CASPT2 level. The exact order of the nπ* and the ππ* states is difficult to establish. Overall the SCS-ADC(2) method has the closest agreement with XMS-CASPT2. However, we refrained from using it for the geometry optimization in the excited state due to the report of the

failure of ADC(2) to describe the CI of carbonyl containing compounds by Curchod and coworkers.[52]

The vertical excitation energies computed with TD-CAM-B3LYP with and without TDA are shown in Fig. S4 and Fig. S5, respectively. These systematically overestimate the excitation energies of the ππ* transition by ~0.4-0.6 eV relative to the XMS-CASPT2 counterparts. Using TDA increases the deviation to ~0.6-0.8 eV (Fig. S5). However, for the nπ* transitions, the deviations of the full TD-DFT and TDA relative to XMS-CASPT2 are similar. For the DPN − CD_{min} model, the latter deviation is ~0.3 eV. For the bigger DPN − CD model, the deviation is sligthly higher and is between ~0.4 - 0.5 eV.

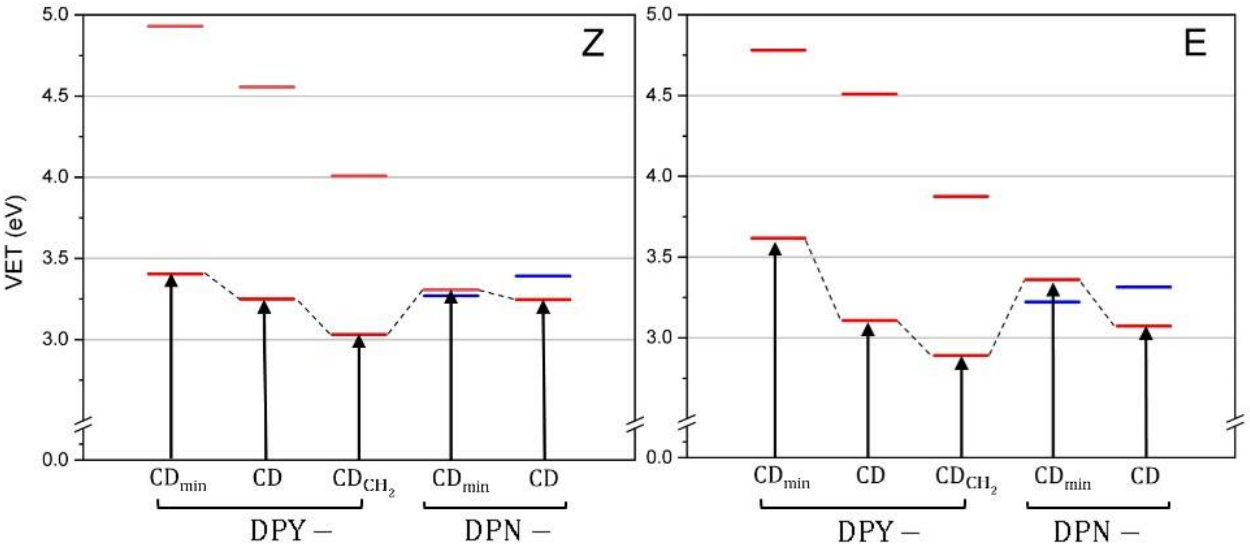

Fig. 6. Vertical excitation energies for all the models at the XMS-CASPT2 level of theory for the *Z* and *E* isomers. The ππ* transitions are shown in red and nπ* transitions are shown in blue.

Photoisomerization profiles at the XMS-CASPT2 level.

DPY − CD_{min} model. The interpolated paths computed for the DPY − CD_{min} model for both the *Z* and *E* isomers are given in Fig. 7. This model lacks both carbonyl and methyl/ethyl groups, which makes it the smallest model studied in this work.

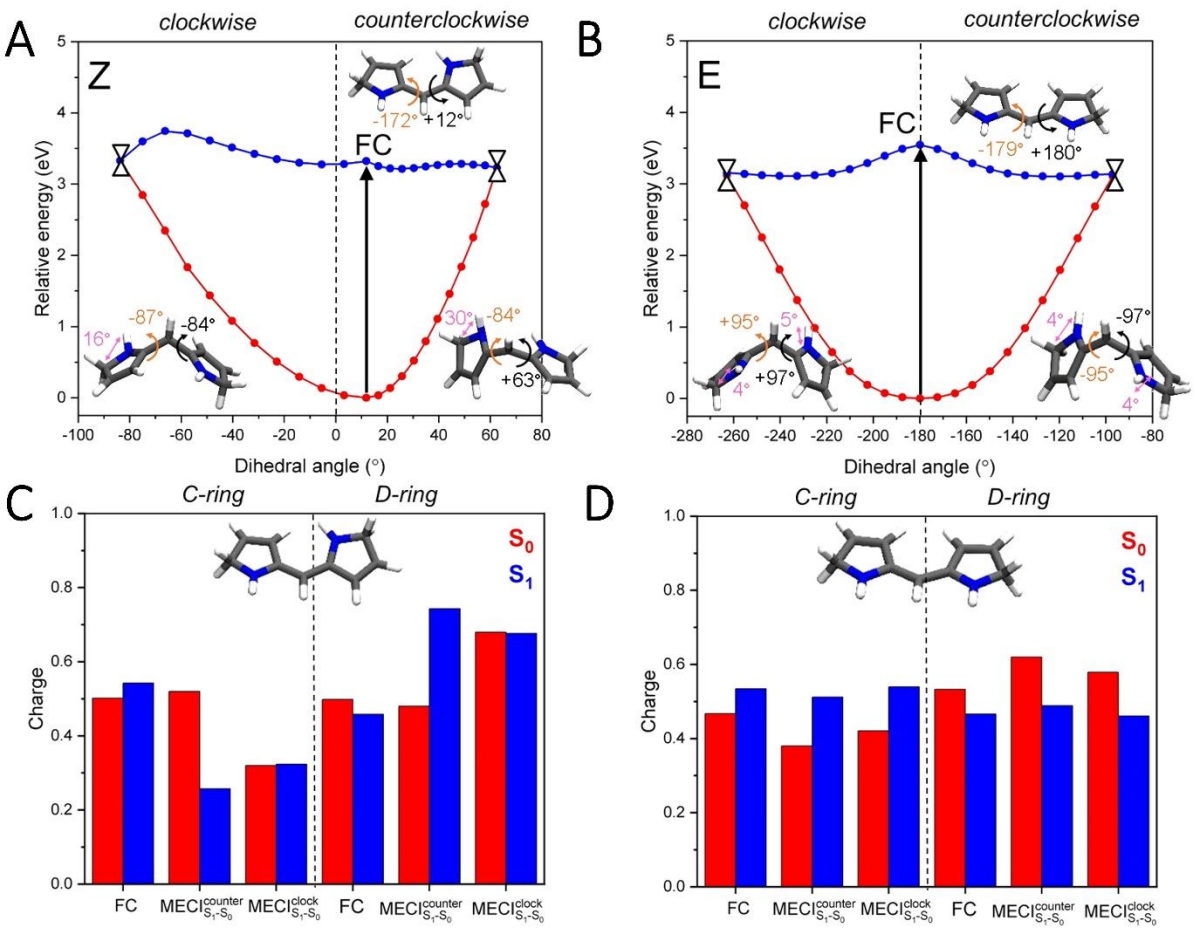

Fig. 7. Photoisomerization profile for the DPY − CD_{min} model. **A, B** Relative energies of the ground and excited state at the XMS-CASPT2/def2-SVP level of theory of the Z and E isomer. The MECIs are indicated for the clockwise and the counterclockwise directions. The geometries of the FC point as well as both MECIs are visualized. The dihedral angle values are shown for ϕ_S and ϕ_D in orange and black, respectively. The pyramidalization at the nitrogen atom greater than 2° is indicated in pink. **C, D** Charge distribution at critical points for both *Z* and *E* isomers.

***Z* isomer.** The ϕ_D dihedral in the $S_{0_{min}}$ geometry is deviating from ideal planarity due to the repulsion between the hydrogen atoms at the pyrrole rings. This repulsion induces a pretwist of the ϕ_D dihedral (12°) which makes the clockwise and counterclockwise rotation different. The counterclockwise path in the S_1state is rather flat with a negligible barrier (0.07 eV) to reach the MECI. This barrier is determined as a difference between the energetically lowest and the highest point of the LIIC in the excited state. The MECI in the counterclockwise direction is 0.09 eV lower than the FC point and has a +63° twist of the ϕ_D dihedral. The clockwise path shows a barrier of

0.47 eV while the MECI is ~0.01 eV lower than the FC point. The clockwise MECI is characterized by a -84° twist of the ϕ_D dihedral. The relaxed scans (Fig. S6) exhibit a excited state profile with a steadily increasing barrier in both directions. However, the scans, failed to reach the MECI since the geometry did not converge after a certain twist of ϕ_D. Hence, on the basis of the LIIC, we deduce that the isomerization in the counterclockwise direction is favoured.

However, in both directions of rotation, the single ($C_{14} - C_{15}$) and double ($C_{15} = C_{16}$) bonds are extending from 1.40 Å to 1.47 Å from the FC point to the MECI. This was also observed along the relaxed scan (Fig. S6) At the MECI point the dihedral $N_C = C_{14} - C_{15} = C_{16}$ (hereafter called ϕ_S, where *S* stands for single bond) is also twisted in addition to the ϕ_D dihedral angle. In clockwise direction, ϕ_S is -87° and ϕ_D is -84°. In the counterclockwise direction these two angles are -84° and +63°, respectively. This is reminiscent of the hula-twist isomerization mechanism[53,54] where these two adjacent bonds isomerize. Due to the concerted twist of two bonds, there is a disruption in the conjugation which leads to a charge redistribution between the C- and D-rings. At the FC point, the charge distribution is close to equal between the C- and D-rings in the ground and the excited states (Fig. 7 C). This indicates a negligible charge transfer upon excitation. But at the MECIs, there is charge transfer between the C- and the D-rings. This points toward a twisted intramolecular charge transfer (TICT)[23]. The positive charge at the C-ring is smaller at the MECI compared to the FC in the excited state (Fig. 7 C). This charge transfer is also reflected in the pyramidalization of 30° and 16° in the counterclockwise and clockwise directions, respectively, at the pyrrole nitrogen of the C-ring. The evaluation of the pyramidalization at the nitrogen atoms N_C and N_D requires the sum of three bond angles involving the N_C and N_D atoms. The sum is subtracted from 360° and the deviation is reported as pyramidalization.

***E* isomer.** The FC geometry of the *E* isomer lacks a pretwist and is planar. Therefore the geometry is nearly symmetric with respect to the molecular plane. As a consequence, both senses of rotation, clockwise and counterclockwise, are identical. The evolution on S_1 is barrierless, leading to MECIs that are ~0.4 eV below the FC point with ϕ_D of -97° and ϕ_S of -95° in the clockwise and counterclockwise directions, respectively. The relaxed scans also exhibit symmetric profiles with a flat excited state topology (Fig. S6). Similar to the *Z* isomer, both $C_{14} - C_{15}$ and $C_{15} = C_{16}$ bond lengths show elongation from 1.40 Å to 1.47 Å (Fig. S6). Another common feature with the *Z*

isomer is a charge transfer at the MECIs in both directions, however, the magnitude is smaller. The same applies to the pyramidalization, which is 4° at the N_C and N_D atoms.

DPY − CD model. This model is obtained by substituting two hydrogen atoms of the C-ring in the DPY − CD_{min} model with methyl groups as well as the two hydrogens of the D-ring with methyl and ethyl groups as in the original chromophore (Fig. 4). Hence, this model is used to study the steric effect of the methyl/ethyl groups on the photoisomerization. The interpolated paths for the DPY − CD model for both the *Z* and *E* isomers are given in Fig. 8.

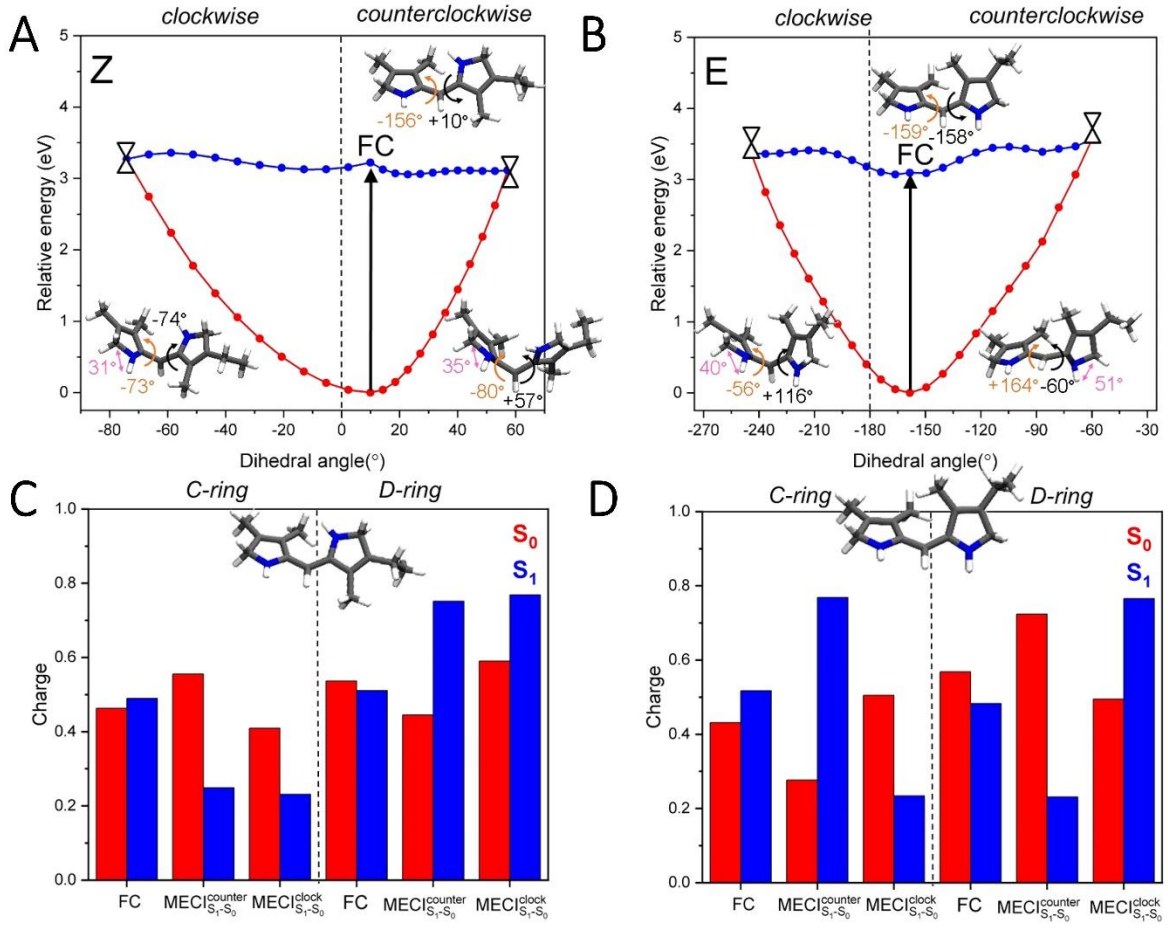

Fig. 8. Photoisomerization profile for the DPY − CD model. **A, B** Relative energies of the ground and excited state at the XMS-CASPT2/def2-SVP level of theory of the Z and E isomer. The MECIs are indicated for the clockwise and the counterclockwise direction. The geometries of the FC point as well as both MECIs are visualized. The dihedral angle values are shown for ϕ_S and ϕ_D in orange and black, respectively. The pyramidalization at the nitrogen atom greater than 2° is indicated in pink. **C, D** Charge distribution at critical points for both *Z* and *E* isomers.

***Z* isomer.** Introduction of methyl groups leads to a slightly decreased ϕ_D of 10° value but a significant increase in the out-of-plane twist of $\phi_S = -156°$ in comparison to the $\mathrm{DPY-CD_{min}}$ model. This can be attributed to the repulsion of the methyl group at the C_{13} atom of the C-ring and the pyrrole group of the D-ring. In the clockwise direction, there is an excited state barrier of 0.23 eV whereas a negligible barrier of 0.06 eV is observed in the counterclockwise direction. The optimized MECIs in the clockwise and counterclockwise directions are similar to those found in the minimal model. They are found to be 0.05 eV and 0.11 eV below the FC point in the clockwise and counterclockwise directions, respectively. The MECI geometries have a ϕ_D twist of -74° and 57° twist and ϕ_S twist of -73° and -80° for clockwise and counterclockwise rotation, respectively. Further, both $C_{14}-C_{15}$ and $C_{15}=C_{16}$ bonds elongate from 1.40 Å to 1.47 Å as described for the $\mathrm{DPY-CD}$ model above. The charge distribution shows a TICT from the C-ring to the D-ring (Fig. 8). A pyramidalization of 31° at the N_C atom of the C-ring was observed in the clockwise direction and 35° in the counterclockwise direction at the corresponding MECI geometries. Similar to the minimal model, the relaxed scans (Fig. S7) show a steadily increasing excited state profile with a failure to reach the MECI. Hence, based on the lower excited state barrier in this model observed in the LIICs, the counterclockwise rotation is more favorable.

***E* isomer.** A significant dihedral pretwist (ϕ_D = -158°) is observed in the *E* isomer of this model, which is a striking difference to the planar *E* isomer of the $\mathrm{DPY-CD_{min}}$ model. This distortion is due to the repulsion between methyl groups at C_{13} of the C-ring and C_{17} of the D-ring. Therefore the LIIC is not symmetric as reported for the minimal model. For this isomer there is a barrier of 0.34 eV while moving from FC to MECI in both directions. The optimized MECIs in the clockwise and counterclockwise directions are at 0.28 eV and 0.47 eV, respectively, above the FC point. At the clockwise MECI the ϕ_S dihedral is -56° and the ϕ_D dihedral is 116°, which indicates a larger rotation around a single bond. In the counterclockwise MECI the ϕ_S and ϕ_D values are 160° and -60°, respectively. Hence, the single bond is nearly planar while the double bond is highly twisted This can also be observed in the relaxed scan (Fig. S7).

A pyramidalization of 51° at the N_D atom of the D-ring and and 40° at the N_C atom of the C-ring is observed in counterclockwise and clockwise directions, respectively. The large pyramidalization might explain the high energy of the counterclockwise MECI. However. the charge distribution is similar to the $\mathrm{DPY-CD_{min}}$ model with a charge transfer between the two rings.

DPY − CD_{CH_2} model. In this model a methylidene group is added to the DPY − CD model. In the full size chromophore there is a carbonyl group at this position and therefore this model serves to test the effect of the substitution of the carbonyl group. The interpolated paths computed for both the *Z* and *E* isomers are given in Fig. 9.

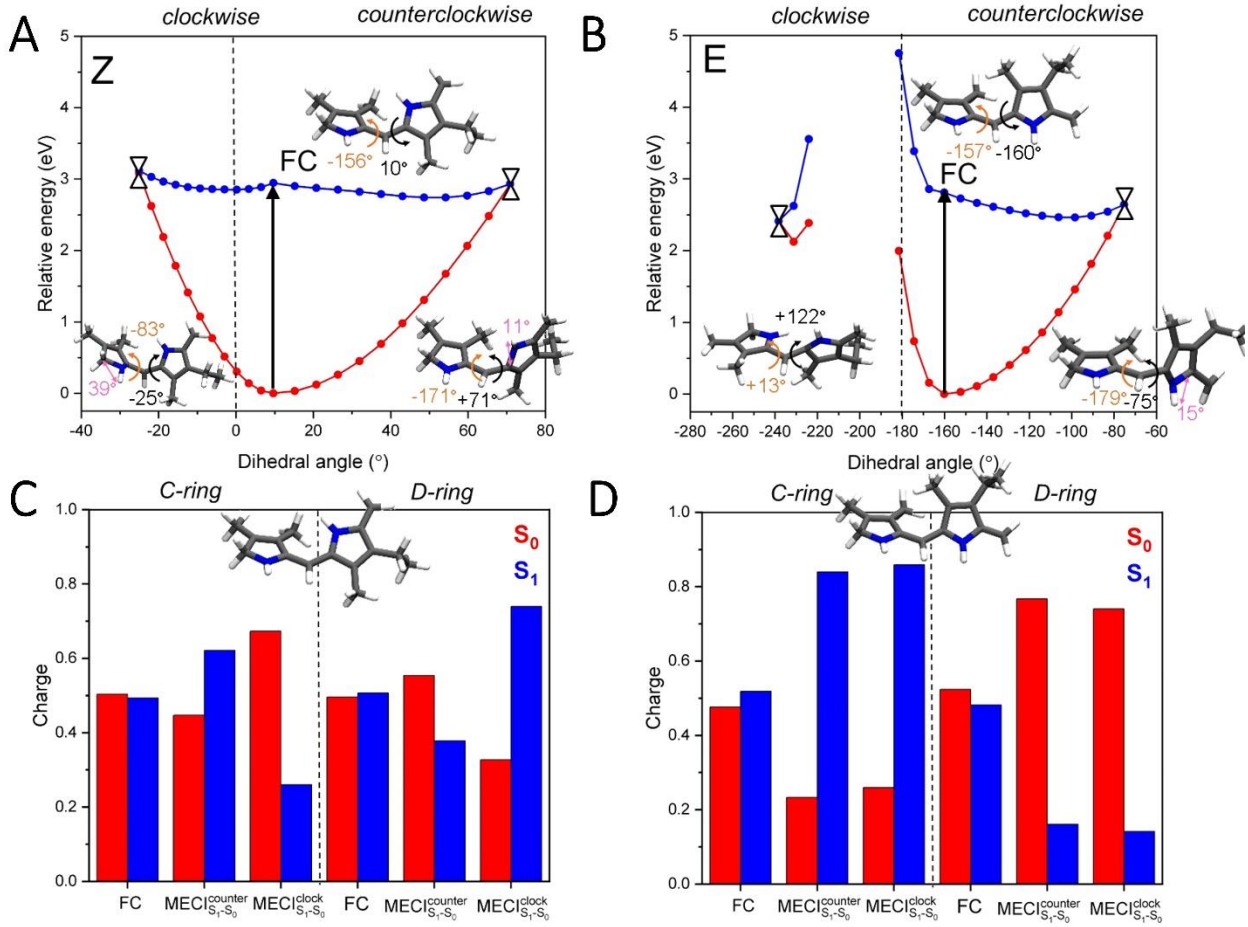

Fig. 9. Photoisomerization profile for the DPY − CD_{CH_2} model. **A, B** Relative energies of the ground and excited state at the XMS-CASPT2/def2-SVP level of theory of the Z and E isomer. The MECIs are indicated for the clockwise and the counterclockwise direction. The geometries of the FC point as well as both MECIs are visualized. The dihedral angle values are shown for ϕ_S and ϕ_D in orange and black, respectively. The pyramidalization at the nitrogen atom greater than 2° is indicated in pink. **C, D** Charge distribution at critical points for both *Z* and *E* isomers.

***Z* isomer.** The pretwist introduced by the methyl groups in the DPY − CD model is also observed in the current model. However, in the clockwise direction the twisting of ϕ_D is associated with a small increase in energyas the MECI is 0.18 eV above the FC point. In the counterclockwise

direction the energy is decreasing and the MECI is below the FC point. The associated geometry is characterized by a twisted double bond but a nearly planar single bond ($\phi_S = -171°$). A pyramidalization of 54° (at the N_C atom) and 11° (at the N_D atom) was observed in the counterclockwise and clockwise directions, respectively. The charge distribution at the MECI in both clockwise and counterclockwise directions shows a smaller charge transfer character compared to the aforementioned models (Fig. 9 C).

***E* isomer.** The pretwist in the ϕ_D dihedral is similar of that in the $\mathrm{DPY-CD}$ model but the rotation of the double bond is barrierless in the counterclockwise rotation and its MECI is 0.17 eV below the FC point. The geometry at the MECI also resembles that of the $\mathrm{DPY-CD}$ model by the fact that only the double bond is twisted. In contrast, the LIIC in the clockwise direction resulted in excited state energies greater than 5 eV which is due to the steric clash between the methyl groups of the two rings. This seems to affect the optimized MECI geometry as well, where the single bond rotated from -157° to +13°. The net rotation of the single bond by 170° resolved the clash between the methyl groups as they are on opposite sides of the *E*-$\mathrm{DPY-CD_{CH_2}}$. To obtain further insight we analysed the relaxed scan in both directions (Fig. S8). The results show no excited state barrier in both senses of rotation. However, the geometrical changes in the clockwise rotation are significantly larger than for the counterclockwise direction. Therefore, we can conclude that the counterclockwise rotation is more likely than the clockwise rotation.

$\mathrm{DPN-CD_{min}}$ model. This is the minimal model with a carbonyl group at the D-ring. This model allows for the isolation of the effect of the carbonyl group on the photoisomerization. The interpolated paths computed for the $\mathrm{DPN-CD_{min}}$ model for both the *Z* and *E* isomers are given in Fig. 10.

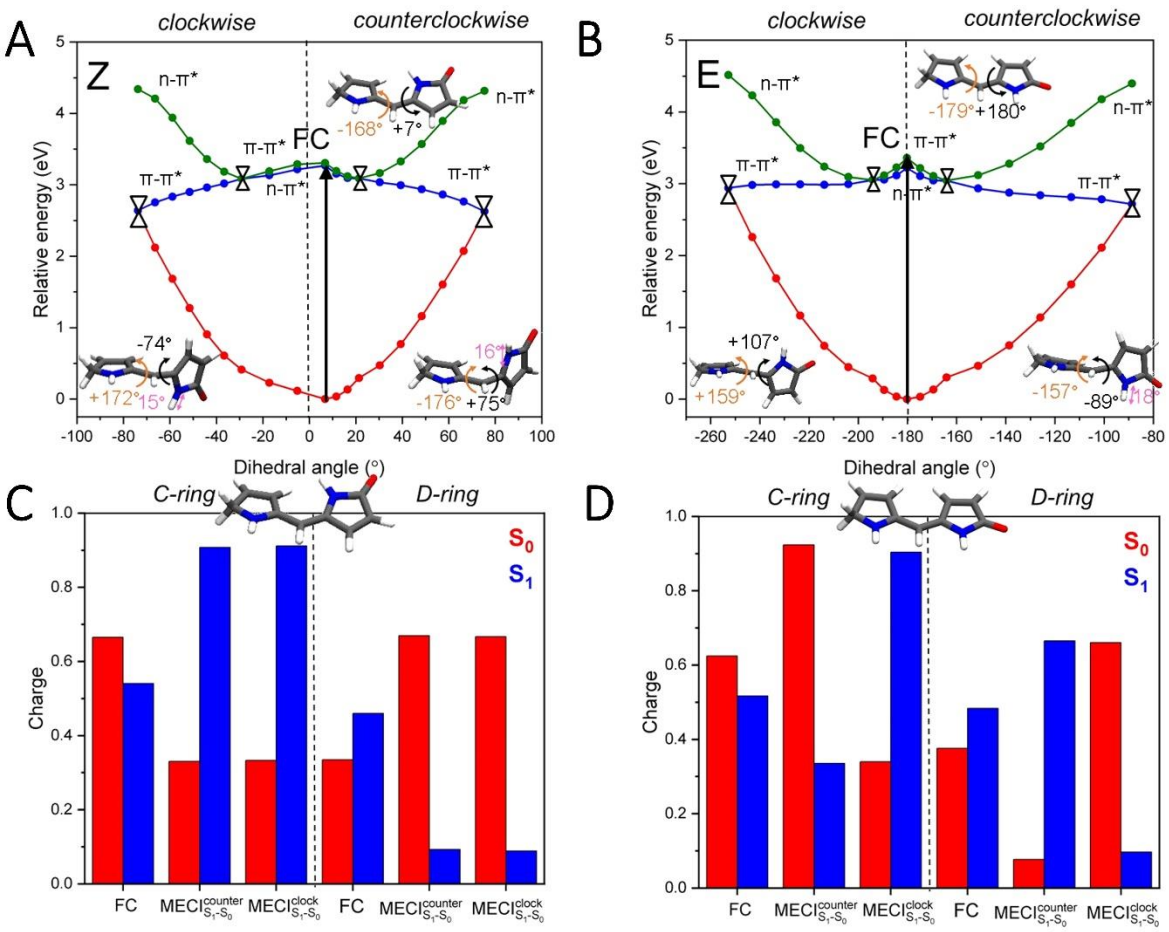

Fig. 10. Photoisomerization profile for the DPN − CD_{min} model. **A, B** Relative energies of the ground and excited state at the XMS-CASPT2/def2-SVP level of theory of the Z and E isomer. The S_1/S_0 MECIs are indicated for the clockwise and the counterclockwise direction. The geometries of the FC point as well as both MECIs are visualized. The dihedral angle values are shown for ϕ_S and ϕ_D in orange and black, respectively. The pyramidalization at the nitrogen atom greater than 2° is indicated in pink. **C, D** Charge distribution at critical points for both *Z* and *E* isomers.

***Z* isomer.** Introduction of the carbonyl group gives rise to a new excited state with nπ* character. It is energetically the lowest excited state (S_1) but it is spectroscopically dark (see section on vertical excitation energies). The next excited state (S_2) is dominated by ππ* character and is therefore spectroscopically bright. The S_2/S_1 MECI is characterized by a ϕ_D value of around ±23° in either direction, where the character of S_2 and S_1 states is interchanged, such that the lowest state is now ππ*. Now the S_1 state evolves barrierless until it reaches the S_2/S_1 MECI in the counterclockwise direction (Fig. 10A). While in the clockwise direction, there is a barrier of 0.17 eV to reach the S_1/S_0 MECI. In both senses of rotation the S_1/S_0 MECI is 0.66 eV below the FC

point. The relaxed scans exhibit barrierless movement in both directions (Fig. S9). At the S_1/S_0 MECI, only the $C_{15} = C_{16}$ bond shows an elongation from 1.38 Å to 1.47 Å (Fig. S9) and a twist of 75° and -74° for clockwise and counterclockwise directions, respectively. The charge distribution at the FC point and the S_1/S_0 MECI shows a strong localization of the positive charge on the C-ring (Fig. 10C).

***E* isomer.** The geometry at the ground state minimum is planar, without a pretwist that was noted in the *Z* isomer. The topology of the excited state profiles is similar to the *Z* isomer, including the initial order of the excited states, their change during the crossing at the S_2/S_1 MECI and the low lying position of the S_1/S_0 MECI with respect to the FC point. In this isomer, both rotations proceed without an excited state barrier which is also observed in the relaxed scan (Fig. S9). The optimized MECIs are characterized by rotation of the $C_{15} = C_{16}$ bond, only. The dihedral ϕ_D is 107° in the clockwise direction and -89° in the counterclockwise direction. Similar to the *Z* isomer, we observe the stretching and rotation of only the $C_{15} = C_{16}$ bond. Despite the similarities between the *E* and *Z* isomer of this model, the charge transfer at the MECI in the clockwise direction is different. The positive charge is localized on the D-ring, instead of C-ring as observed in the *Z* isomer. However, for the counterclockwise isomerization the positive charge is localized on the C-ring (Fig. 10D).

DPN − CD model. This model is the most complete in terms of functional groups of the C- and D-rings with respect to the PCB chromophore due to the addition of the methyl/ethyl groups along with the carbonyl group at the D-ring. The interpolated paths are given in Fig. 11.

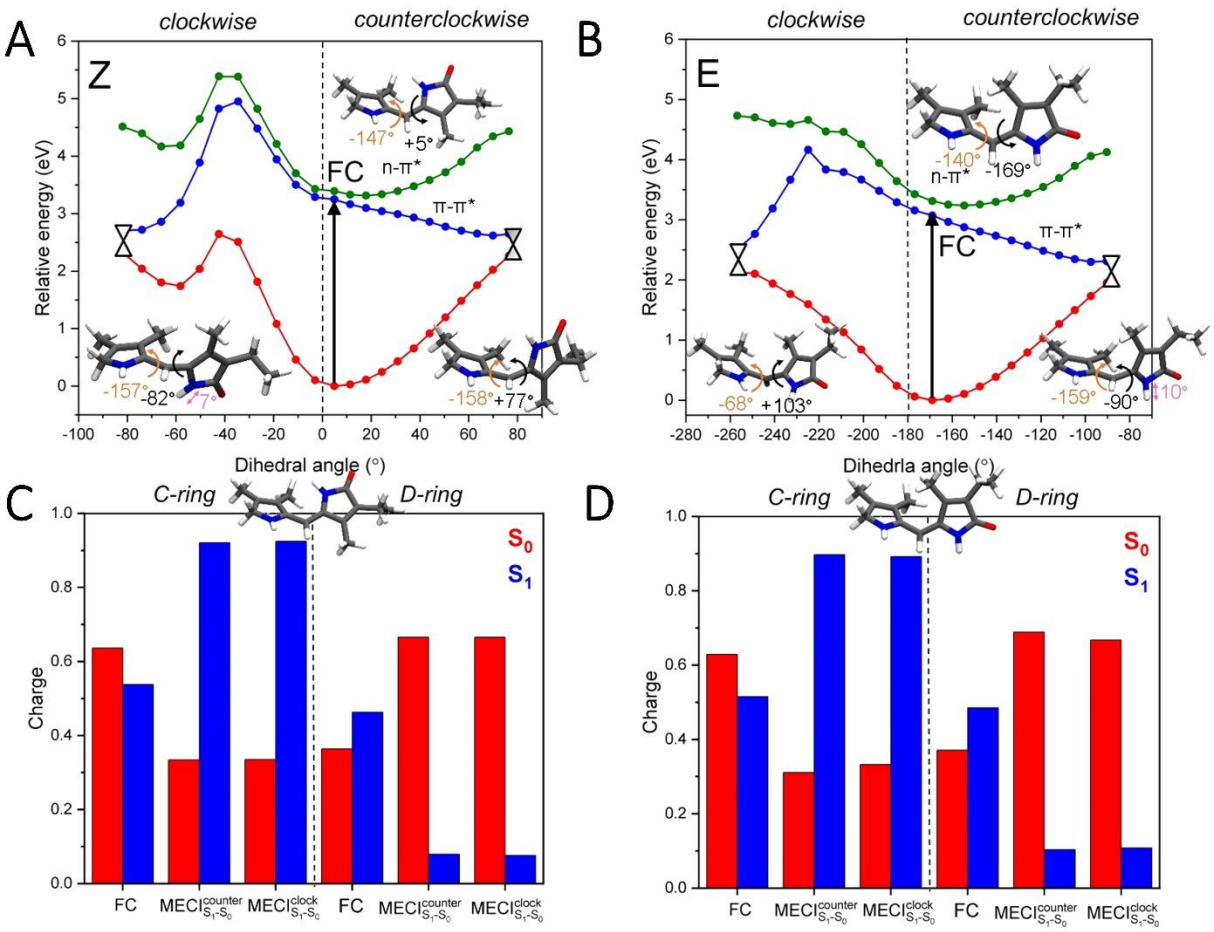

Fig. 11 Photoisomerization profile for the DPN − CD model. **A, B** Relative energies of the ground and excited state at the XMS-CASPT2/def2-SVP level of theory of the Z and E isomer. The S_1/S_0 MECIs are indicated for the clockwise and the counterclockwise direction. The geometries of the FC point as well as both MECIs are visualized. The dihedral angle values are shown for ϕ_S and ϕ_D in orange and black, respectively. The pyramidalization at the nitrogen atom greater than 2° is indicated in pink. **C, D** Charge distribution at critical points for both *Z* and *E* isomers.

***Z* isomer.** The double bond pretwist exhibited by the FC geometry ($\phi_D = 5°$) is smaller compared to the previous models. However, the single bond shows the largest torsion among all *Z* isomers studied in this work. The first spectroscopically bright state is S_1 with ππ* character, in contrast to the DPN − $\mathrm{CD_{min}}$ model, where S_1 is dark with nπ* character. The counterclockwise rotation is barrierless leading to the S_1/S_0 MECI which is 0.60 eV lower than the FC point. In the clockwise rotation the S_1/S_0 MECI is 0.53 eV below the FC point, however, the interpolation leads to an increase in the barrier owing to the repulsion between the methyl groups. This leads to a problem since geometry relaxation is not accounted for in the linear interpolation. In fact, the relaxed scan

shows no barrier in both senses of rotation (Fig. S10). Similar to the $\mathrm{DPN-CD_{min}}$ model, the twisting is observed only along the double bond which is found for some models without the carbonyl group. The charge distribution shows localized positive charge on the C-ring. Except for a minor value of 7° observed at the N_C atom of C-ring there is no larger pyramidalization like in the previously discussed models.

***E* isomer.** The FC geometry exhibits a reduced double bond pretwist (ϕ_D = -169°) with the largest single bond rotation (ϕ_S = -140°) compared to the previous models with methyl groups. Similar to the *Z*-isomer, the S_1 state is bright and has a ππ* character. The counterclockwise rotation is barrierless leading to the CI which is 0.76 eV lower than the FC point. Similar to the *Z* isomer, a clockwise rotation introduces a large barrier due to the artifact of the linear interpolation. The artifact is introduced by the absence of geometric relaxation as discussed above. Also, the relaxed scan shows a steep increase in the excited state energy (Fig. S10). Interestingly, the S_1/S_0 MECI is well below (0.56 eV) the FC point. This could be due to a rearrangement needed to overcome the clash of methyl groups. The charge distribution at the MECI indicated that for both MECIs the positive charge is localized on the C-ring.

Discussion and Conclusions

In this work, we studied the photochemical deactivation of phytochrome chromophore models using LIICs between the FC and the MECI geometries. Summary of important geometric parameters and excited state barrier heights observed in the LIICs of both *Z* and *E* isomers are given in Table S3 and S4, respectively. First, we established the relative order of the excited states in the chromophore models. In the case of the DPY-type models, the first excited state has ππ* character and is spectroscopically bright. Therefore, the S_1.state was chosen for the calculation of the MECI and the subsequent photoisomerization profiles. However, in case of the DPN-type models there is an additional low-lying excited state due to the introduction of a carbonyl group. The latter state is dominated by nπ* character and is energetically close to the ππ* state. For *Z* and *E* isomers of $\mathrm{DPN-CD_{min}}$ this state was energetically lower than the ππ* state, which required the optimization of an additional MECI between S_2 and S_1. However, along the interpolation, the latter two states cross at smaller twisting angles of ±23°. The presence of the nπ* state is due to the truncation of the PCB chromophore and hence in a bigger model we expect that the ππ* state to be lower in energy.

The photoisomerization profile of $\mathrm{DPY-CD_{min}}$ indicated a barrierless access to the MECI for the *E* isomer in clockwise and counterclockwise directions due to a planar ground state geometry. On the contrary, a pretwist is observed within the corresponding geometry of the *Z* isomer that creates a preference for the isomerization in the counterclockwise sense of rotation. This preference is due to the steric repulsion between the hydrogen atoms of the two rings which increases systematically in the *Z* and *E* isomers of $\mathrm{DPY-CD}$ and $\mathrm{DPY-CD_{CH_2}}$ models upon introduction of methyl and ethyl groups. Accordingly, a barrierless movement (or a negligible excited state barrier) is observed in the counterclockwise direction in both $\mathrm{DPY-CD}$ and $\mathrm{DPY-CD_{CH_2}}$ models, compared to the clockwise direction. In addition, the MECIs of the *E* isomer of $\mathrm{DPY-CD}$ are energetically higher than the FC point. A similar observation is made in the $\mathrm{DPY-CD_{CH_2}}$ model for the the MECI in the clockwise direction which is 0.18 eV above the FC point. Moreover, the LIIC for the clockwise isomerization in the latter model leads to a clash of methyl groups resulting in an energy increase. In the study by Dean and coworkers[27], it is reported that the DPY model relaxes to the ground state with a time constant of 0.46 ps. This is in line with our finding of a small excited state barrier of 0.06 eV in the counterclockwise direction. However, it should be noted that the structure of the model is slightly different and the experiment was performed in methanol, while our simulation is done in the gas phase.

The introduction of the carbonyl group in the $\mathrm{DPN-CD_{min}}$ and $\mathrm{DPN-CD}$ models leads to MECIs that are energetically lower than those found for the DPY-type models. The interpolated pathways are barrierless, except for the clockwise path of both isomers of the $\mathrm{DPN-CD}$ model. However, this is an artifact arising from the lack of geometric relaxation in the LIIC paths. Interestingly, all MECIs are characterized by the rotations of only the double bond of the methine bridge, while the single bond shows only a minor twist. Hence, the isomerization mechanism changes from a hula-twist as observed in the DPY-type models to a one-bond flip in the DPN-type models. This can be rationalized by a larger amount of charge transfer compared to the models without the carbonyl group. The different charge distribution is also reflected in a reduced extent of pyramidalization at the N_C and N_D atoms.

While the presented models are truncated and the environmental effect is neglected in our simulations, there is one general observation that can be transferred to the photoisomerization in phytochromes. The paths of models with methyl groups have revealed a pretwist and a preference

for counterclockwise double bond rotation. The preference for the counterclockwise rotation appears to be an intrinsic property of the tetrapyrrole chromophore due to steric repulsion between the methyl groups at the C- and D- rings. This preference has also been reported in QM/MM studies of various phytochromes.[20,22,32,33] This work can serve as a guide for future experimental and computational studies on the excited state dynamics of truncated tetrapyrroles. In addition, the study can also serve as a reference in benchmarks of computational methods since the current study demonstrates that the XMS-CASPT2 method can effectively describe CIs in these systems.

Acknowledgments. This work is supported by the German Research Foundation via SFB 1078 (project C6) and European Research Council (ERC) under the European Union's Horizon 2020 research and innovation programme (grant agreement No 678169, ERC Starting Grant "PhotoMutant").

Supplementary Information. Vertical excitation energies, excited state relaxed scans and a summary of important parameters from LIICs can be found.

References

1 N. C. Rockwell, Y.-S. Su and J. C. Lagarias, *Annu. Rev. Plant Biol.*, 2006, **57**, 837–858.

2 N. C. Rockwell and J. C. Lagarias, *ChemPhysChem*, 2010, **11**, 1172–1180.

3 I. Schapiro, F. Melaccio, E. N. Laricheva and M. Olivucci, *Photochem. Photobiol. Sci.*, 2011, **10**, 867–886.

4 S. Gozem, H. L. Luk, I. Schapiro and M. Olivucci, *Chem. Rev.*, 2017, **117**, 13502–13565.

5 Y. Fukushima, M. Iwaki, R. Narikawa, M. Ikeuchi, Y. Tomita and S. Itoh, *Biochemistry*, 2011, **50**, 6328–6339.

6 J. Dasgupta, R. R. Frontiera, K. C. Taylor, J. C. Lagarias and R. A. Mathies, *Proc. Natl. Acad. Sci.*, 2009, **106**, 1784–1789.

7 K. Heyne, J. Herbst, D. Stehlik, B. Esteban, T. Lamparter, J. Hughes and R. Diller, *Biophys. J.*, 2002, **82**, 1004–1016.

8 K. C. Toh, E. A. Stojković, A. B. Rupenyan, I. H. M. van Stokkum, M. Salumbides, M.-L.

Groot, K. Moffat and J. T. M. Kennis, *J. Phys. Chem. A*, 2011, **115**, 3778–3786.

9 J. S. Kirpich, L. T. Mix, S. S. Martin, N. C. Rockwell, J. C. Lagarias and D. S. Larsen, *J. Phys. Chem. Lett.*, 2018, **9**, 3454–3462.

10 D. Wang, X. Li, L. Wang, X. Yang and D. Zhong, *J. Phys. Chem. Lett.*, 2020, **11**, 8819–8824.

11 B. Durbeej, *Phys. Chem. Chem. Phys.*, 2009, **11**, 1354–1361.

12 A. Strambi and B. Durbeej, *Photochem. Photobiol. Sci.*, 2011, **10**, 569–579.

13 M. Huix-Rotllant, M. Filatov, S. Gozem, I. Schapiro, M. Olivucci and N. Ferré, *J. Chem. Theory Comput.*, 2013, **9**, 3917–3932.

14 B. G. Levine, C. Ko, J. Quenneville and T. J. Martínez, *Mol. Phys.*, 2006, **104**, 1039–1051.

15 D. Roca-Sanjuán, F. Aquilante and R. Lindh, *WIREs Comput. Mol. Sci.*, 2012, **2**, 585–603.

16 M. Boggio-Pasqua and G. Groenhof, *Comput. Theor. Chem.*, 2014, **1040**–**1041**, 6–13.

17 C. M. Jones, N. H. List and T. J. Martínez, *J. Am. Chem. Soc.*, 2022, **144**, 12732–12746.

18 J. R. Church, A. G. Rao, A. Barnoy, C. Wiebeler and I. Schapiro, *QM/MM Stud. Light. Biol. proteins.,T. Andruniow M. Olivucci, eds.*, 197–226.

19 F. Aquilante, J. Autschbach, R. K. Carlson, L. F. Chibotaru, M. G. Delcey, L. De Vico, I. Fdez. Galván, N. Ferré, L. M. Frutos, L. Gagliardi, M. Garavelli, A. Giussani, C. E. Hoyer, G. Li Manni, H. Lischka, D. Ma, P. Å. Malmqvist, T. Müller, A. Nenov, M. Olivucci, T. B. Pedersen, D. Peng, F. Plasser, B. Pritchard, M. Reiher, I. Rivalta, I. Schapiro, J. Segarra-Martí, M. Stenrup, D. G. Truhlar, L. Ungur, A. Valentini, S. Vancoillie, V. Veryazov, V. P. Vysotskiy, O. Weingart, F. Zapata and R. Lindh, *J. Comput. Chem.*, 2016, **37**, 506–541.

20 X. Zhuang, J. Wang and Z. Lan, *J. Phys. Chem. B*, 2013, **117**, 15976–15986.

21 H. Huang, C. Xu, K. Lin, J. Peng, F. L. Gu and Z. Lan, *ChemRxiv*, 2022, 1–7.

22 G. Salvadori, V. Macaluso, G. Pellicci, L. Cupellini, G. Granucci and B. Mennucci, *ChemRxiv*, 2022, 1–31.

23 P. Altoé, T. Climent, G. C. De Fusco, M. Stenta, A. Bottoni, L. Serrano-Andrés, M. Merchán, G. Orlandi and M. Garavelli, *J. Phys. Chem. B*, 2009, **113**, 15067–15073.

24 B. Durbeej, *Phys. Chem. Chem. Phys.*, 2009, **11**, 1354–1361.

25 A. Strambi and B. Durbeej, *Photochem. Photobiol. Sci.*, 2011, **10**, 569–579.

26 S. Kaminski, G. Daminelli and M. A. Mroginski, *J. Phys. Chem. B*, 2009, **113**, 945–958.

27 C. F. Staheli, J. Barney, T. R. Clark, M. Bowles, B. Jeppesen, D. G. Oblinsky, M. B. Steffensen and J. C. Dean, *Front. Chem.*, 2021, **9**, 1–15.

28 B. Zietz and F. Blomgren, *Chem. Phys. Lett.*, 2006, **420**, 556–561.

29 J. Janoš, D. Madea, S. Mahvidi, T. Mujawar, J. Švenda, J. Suchan, P. Slavíček and P. Klán, *J. Phys. Chem. A*, 2020, **124**, 10457–10471.

30 P. Altoé, T. Climent, G. C. De Fusco, M. Stenta, A. Bottoni, L. Serrano-Andrés, M. Merchán, G. Orlandi and M. Garavelli, *J. Phys. Chem. B*, 2009, **113**, 15067–15073.

31 E. Claesson, W. Y. Wahlgren, H. Takala, S. Pandey, L. Castillon, V. Kuznetsova, L. Henry, M. Panman, M. Carrillo, J. Kübel, R. Nanekar, L. Isaksson, A. Nimmrich, A. Cellini, D. Morozov, M. Maj, M. Kurttila, R. Bosman, E. Nango, R. Tanaka, T. Tanaka, L. Fangjia, S. Iwata, S. Owada, K. Moffat, G. Groenhof, E. A. Stojković, J. A. Ihalainen, M. Schmidt and S. Westenhoff, *Elife*, 2020, **9**, 1–18.

32 C. Slavov, T. Fischer, A. Barnoy, H. Shin, A. G. Rao, C. Wiebeler, X. Zeng, Y. Sun, Q. Xu, A. Gutt, K. H. Zhao, W. Gärtner, X. Yang, I. Schapiro and J. Wachtveitl, *Proc. Natl. Acad. Sci. U. S. A.*, 2020, **117**, 16356–16362.

33 D. Morozov, V. Modi, V. Mironov and G. Groenhof, *J. Phys. Chem. Lett.*, 2022, **13**, 4538–4542.

34 T. Shiozaki, *Wiley Interdiscip. Rev. Comput. Mol. Sci.*, 2018, **8**, 1–7.

35 J. W. Park and T. Shiozaki, *J. Chem. Theory Comput.*, 2017, **13**, 2561–2570.

36 C. García-Iriepa, H. A. Ernst, Y. Liang, A.-N. Unterreiner, L. M. Frutos and D. Sampedro, *J. Org. Chem.*, 2016, **81**, 6292–6302.

37 D. Madea, T. Mujawar, A. Dvořák, K. Pospíšilová, L. Muchová, P. Čubáková, M. Kloz, J. Švenda, L. Vítek and P. Klán, *J. Org. Chem.*, 2022, **87**, 3089–3103.

38 I. Lyskov, A. Anda, Y. X. Wong, A. J. Tilley, C. R. Hall, J. Thia, S. P. Russo, W. W. H. Wong, J. H. Cole and T. A. Smith, *Phys. Chem. Chem. Phys.*, 2020, **22**, 15567–15572.

39 S. Metz, J. Kästner, A. A. Sokol, T. W. Keal and P. Sherwood, *Wiley Interdiscip. Rev. Comput. Mol. Sci.*, 2014, **4**, 101–110.

40 T. Yanai, D. P. Tew and N. C. Handy, *Chem. Phys. Lett.*, 2004, **393**, 51–57.

41 J. Schirmer, *Phys. Rev. A*, 1982, **26**, 2395–2416.

42 A. Hellweg, S. A. Grün and C. Hättig, *Phys. Chem. Chem. Phys.*, 2008, **10**, 4119–4127.

43 S. Grimme, *J. Chem. Phys.*, 2003, **118**, 9095–9102.

44 Y. Jung, R. C. Lochan, A. D. Dutoi and M. Head-Gordon, *J. Chem. Phys.*, 2004, **121**, 9793–9802.

45 M. J. Frisch, G. W. Trucks, H. B. Schlegel, G. E. Scuseria, M. A. Robb, J. R. Cheeseman, G. Scalmani, V. Barone, B. Mennucci, G. A. Petersson, H. Nakatsuji, M. Caricato, X. Li, H. P. Hratchian, A. F. Izmaylov, J. Bloino, G. Zheng, J. L. Sonnenberg, M. Hada, M. Ehara, K. Toyota, R. Fukuda, J. Hasegawa, M. Ishida, T. Nakajima, Y. Honda, O. Kitao, H. Nakai, T. Vreven, J. A. Montgomery Jr., J. E. Peralta, F. Ogliaro, M. Bearpark, J. J. Heyd, E. Brothers, K. N. Kudin, V. N. Staroverov, T. Keith, R. Kobayashi, J. Normand, K. Raghavachari, A. Rendell, J. C. Burant, S. S. Iyengar, J. Tomasi, M. Cossi, N. Rega, J. M. Millam, M. Klene, J. E. Knox, J. B. Cross, V. Bakken, C. Adamo, J. Jaramillo, R. Gomperts, R. E. Stratmann, O. Yazyev, A. J. Austin, R. Cammi, C. Pomelli, J. W. Ochterski, R. L. Martin, K. Morokuma, V. G. Zakrzewski, G. A. Voth, P. Salvador, J. J. Dannenberg, S. Dapprich, A. D. Daniels, O. Farkas, J. B. Foresman, J. V. Ortiz, J. Cioslowski and D. J. Fox, 2013.

46 F. Furche, R. Ahlrichs, C. Hättig, W. Klopper, M. Sierka and F. Weigend, *Wiley*

Interdiscip. Rev. Comput. Mol. Sci., 2014, **4**, 91–100.

47 F. Bernardi, M. Olivucci and M. A. Robb, *Chem. Soc. Rev.*, 1996, **25**, 321–328.

48 B. G. Levine, J. D. Coe and T. J. Martínez, *J. Phys. Chem. B*, 2008, **112**, 405–413.

49 H. Lischka, T. Müller, P. G. Szalay, I. Shavitt, R. M. Pitzer and R. Shepard, *WIREs Comput. Mol. Sci.*, 2011, **1**, 191–199.

50 H. Lischka, R. Shepard, R. M. Pitzer, I. Shavitt, M. Dallos, T. Müller, P. G. Szalay, M. Seth, G. S. Kedziora, S. Yabushita and Z. Zhang, *Phys. Chem. Chem. Phys.*, 2001, **3**, 664–673.

51 H. Lischka, R. Shepard, I. Shavitt, R. M. Pitzer, M. Dallos, T. Müller, P. G. Szalay, F. B. Brown, R. Ahlrichs, H. J. Böhm, A. Chang, D. C. Comeau, R. Gdanitz, H. Dachsel, C. Ehrhardt, M. Ernzerhof, P. Höchtl, S. Irle, G. Kedziora, T. Kovar, V. Parasuk, M. J. M. Pepper, P. Scharf, H. Schiffer, M. Schindler, M. Schüler, M. Seth, E. A. Stahlberg, J.-G. Zhao, S. Yabushita, Z. Zhang, M. Barbatti, S. Matsika, M. Schuurmann, D. R. Yarkony, S. R. Brozell, E. V. Beck, and J.-P. Blaudeau, M. Ruckenbauer, B. Sellner, F. Plasser, J. J. Szymczak, R. F. K. Spada and A. Das, *COLUMBUS, an ab initio Electron. Struct. program, release 7.0*, 2017.

52 E. Marsili, A. Prlj and B. F. E. Curchod, *Phys. Chem. Chem. Phys.*, 2021, **23**, 12945–12949.

53 R. S. H. Liu and G. S. Hammond, *Proc. Natl. Acad. Sci.*, 2000, **97**, 11153–11158.

54 S. Sen, R. K. Kar, V. A. Borin and I. Schapiro, *WIREs Comput. Mol. Sci.*, 2022, **12**, e1562.